

Unidirectional disorder-immune transmission and reconfigurable route of Fermi arcs in photonic topological Weyl metamaterials

Mingzhu Li¹,[✉] Ning Han,¹ Jie Song,^{1,*} and Yongyuan Jiang^{1,2,3,4,†}

¹*School of Physics, Harbin Institute of Technology, Harbin 150001, China*

²*Collaborative Innovation Center of Extreme Optics, Shanxi University, Taiyuan 030006, China*

³*Key Lab of Micro-Optics and Photonic Technology of Heilongjiang Province, Harbin 150001, China*

⁴*Key Lab of Micro-Nano Optoelectronic Information System, Ministry of Industry and Information Technology, Harbin 150001, China*



(Received 14 February 2022; revised 5 July 2022; accepted 22 July 2022; published 2 August 2022)

In this paper, we demonstrate the existence of multiple photonic Fermi arcs with the same transmission direction at the interface between two different topological Weyl media. The surface waves are not affected by the type and number of defects and can bypass defects for robust one-way transportation, which confirms the disorder-immune property of Fermi arcs. The reconfigurable routing of Fermi arc surface waves can be well realized by changing the gyromagnetic and chiral parameters of Weyl metamaterials in H-shaped channels. Moreover, the unidirectional excitation and controllable transmission of Fermi arcs can be realized by adopting the different signs of the propagation constant and different interface configurations in T-shaped channels. Our paper provides an insight into the topological properties of Fermi arcs between two topological Weyl systems.

DOI: [10.1103/PhysRevB.106.075301](https://doi.org/10.1103/PhysRevB.106.075301)

I. INTRODUCTION

Weyl semimetal is a new topological state of matter supporting emergent topologically protected nontrivial band-crossing points, which are known as Weyl points [1–3]. In the last few years, topological materials hosting Weyl points have become a research hotspot in the field of electron-related systems [4–6], electromagnetic systems [7–9], and acoustic systems [10–12]. Weyl points can be viewed as the magnetic monopole in momentum space and act as the sources and sinks of the Berry curvatures [13,14]. Generally, the Hamiltonian of a Weyl point possesses the form $H = v_x k_x \sigma_x + v_y k_y \sigma_y + v_z k_z \sigma_z$ [15–17], where v_i , σ_i , and k_i ($i = x, y, z$) are the Fermi velocity, the Pauli matrices, and the wave vectors along the x , y , and z axes, respectively. Note that the Weyl Hamiltonian contains all three Pauli matrices and exhausts all the allowable degrees of freedom. Therefore, Weyl points are almost indestructible, unless a pair of Weyl points with opposite topological charges annihilate each other [18,19].

In fact, the generation of Weyl points requires breaking the time-reversal or spatial inversion symmetry, or both [20,21]. Particularly, Wang *et al.* report the experimental observation of photonic Weyl degeneracies (terahertz) in a magnetized semiconductor InSb [22]. The Nielsen-Ninomiya no-go theorem [23] ensures that Weyl points appear in pairs with opposite charges. For instance, in a system that maintains spatial inversion symmetry, the Berry curvatures satisfy $\Omega(\mathbf{k}) = \Omega(-\mathbf{k})$ [24]. It dictates a Weyl point located at \mathbf{k} to have the opposite topological charge as its partner point at $-\mathbf{k}$ [25]. Thus, the minimum number of Weyl points in this case is 2,

including a positive and a negative charge. In contrast, under a time-reversal symmetry invariant system, the Berry curvatures meet the relation $\Omega(\mathbf{k}) = -\Omega(-\mathbf{k})$ [26]. In other words, a Weyl point at \mathbf{k} has the same topological charge as its companion point at $-\mathbf{k}$ [27]. Because the total net charge of the system must be zero, another pair of Weyl points with opposite charges is required to be present. Therefore, the minimum number of Weyl points is 4 for this system [28]. Additionally, according to whether the conelike band structure at the Weyl points is tilted or not [29,30], Weyl semimetals can be divided into three types. A standard (type-I) Weyl point possesses a pointlike Fermi surface [31]. On the other hand, the unconventional type-II Weyl point appears as a strongly tilted cone dispersion [32,33]. In particular, the critical-type Weyl point is present exactly at the critical transition between the type-I and type-II Weyl point [22,34]. All types of Weyl points are topologically nontrivial. In addition, Weyl semimetals exhibit extraordinary transport properties. Consequently, they have caught growing attention and have been widely studied in condensed matter, photonic, and phononic systems [35–38].

In Weyl semimetals, bulk-surface correspondence guarantees the existence of Fermi arc surface states at the interfaces between two topologically different materials [39–41]. A nontrivial Fermi arc is the salient signature of topological property in Weyl semimetals, which connects the projection of Weyl points of opposite chirality [41]. The topological strength can be measured by the length of the Fermi arc [42]. Investigation on Fermi arcs lays a foundation for understanding the new physics of nontrivial topological semimetals and may have potential in device applications [43]. In condensed matter systems, the topologically protected Fermi arcs exhibit unconventional quantum oscillations, magnetoresistance, anomalous quantum interference effects, magnetic transport, and chiral magnetic effects [44–46]. On the other

*jsong@hit.edu.cn

†jiangy@hit.edu.cn

hand, in classical wave systems, researchers have studied the transmission characteristics of Fermi arc surface states in Weyl semimetals, including topological negative refraction [47], vortical reflection [48], topological one-way fibers [49], and optical pulling [50].

It is well known that symmetry plays an important role in the physics of topological materials. Symmetry-based indicators have proved to be a powerful theoretical tool for diagnosing and predicting topological semimetals [51–53]. Recently, three-dimensional photonic topological Weyl degeneracies have been studied in both the gyromagnetic metamaterials [21] and chiral metamaterials [34]. Their topological natures are significantly different. The time-reversal symmetry of the gyromagnetic metamaterial is broken due to the gyromagnetic effect [21]. In contrast, the introduction of the chiral effect breaks the spatial inversion symmetry of the chiral metamaterials [34]. In particular, our two previous works focused on the physics of Weyl points in gyromagnetic and chiral metamaterials, demonstrating the existence of a Fermi arc at the interface between Weyl metamaterials and vacuum. Moreover, the chiral effects can exist in a range of natural media [54], and the development of metamaterials allows us to synthesize strong chiral materials [55]. On the other hand, to realize the gyromagnetic effects, magnetic media are mixed during fabrication and one commonly used medium is yttrium-iron-garnet [56]. Now, the Fermi arc surface states have been studied in photonic crystals [7], phononic crystals [47], and photonic metamaterials [15]. However, there are few studies on the Fermi arc surface states at the interface between two different Weyl materials. Therefore, two questions naturally arise. Can we realize the Fermi arc surface states in the boundary of two Weyl materials with different symmetry-protection mechanisms in one photonic system? If so, what interesting phenomena will this novel topological configuration bring?

In this paper, building on our previous work [21], we focus on the copropagating photonic Fermi arcs and their transport properties hosted by the interface between the gyromagnetic and the chiral metamaterials. Both materials possess topological protected critical-type Weyl points. Remarkably, the whole system can support two Fermi arcs with the same propagation direction because of bulk-surface correspondence. Particularly, we demonstrate the existence of Weyl exceptional contours in Weyl metamaterials while considering losses and further explore and analyze the phase diagrams of the system transitioning from the Weyl semimetal phase to the trivial phase. Multiple copropagating surface channels can be used for the unidirectional excitation and robust information mixing of waves [35]. Therefore, we construct H-shaped and T-shaped waveguide configurations by backscattering immune Fermi arcs for multiplexing and controllable routing. Our paper is helpful to clarify the related potential applications of the copropagating photonic Fermi arc surface states in the field of photonics.

This paper is organized as follows. In Sec. II, we show the band structures and Fermi arcs for the gyromagnetic and chiral metamaterials. In Sec. III, we exhibit the multiplexing of surface waves across the H-shaped channel. In Sec. IV, The topologically protected Fermi arc surface state can propagate nonreciprocally on the T junction. In Sec. V, we analyze the

Weyl exceptional contours and the phase diagrams in Weyl metamaterials while considering losses. The conclusion is given in Sec. VI.

II. BAND STRUCTURES AND FERMION ARCS FOR GYROMAGNETIC AND CHIRAL METAMATERIALS

Topological metamaterials based on effective medium theory can be regarded as homogeneous media [37]. Particularly, the topological phases can be induced by adjusting the effective parameters of the metamaterials. The most general form of the constitutive equation can be written as

$$\begin{pmatrix} \mathbf{D} \\ \mathbf{B} \end{pmatrix} = \begin{pmatrix} \epsilon_0 \bar{\epsilon}_{r(r=1,2)} & i\sqrt{\epsilon_0 \mu_0} \bar{\xi}_{r(r=1,2)} \\ i\sqrt{\epsilon_0 \mu_0} \bar{\eta}_{r(r=1,2)} & \mu_0 \bar{\mu}_{r(r=1,2)} \end{pmatrix} \begin{pmatrix} \mathbf{E} \\ \mathbf{H} \end{pmatrix}, \quad (1)$$

where ϵ_0 and μ_0 are the permittivity and permeability of vacuum, respectively. For simplicity, we set $\epsilon_0 = \mu_0 = 1$. $\bar{\xi}$ and $\bar{\eta}$ are cross tensors associated with the magnetoelectric coupling.

The topological properties of the gyromagnetic metamaterials can be determined by the constitutive equations, and the constitutive matrices are given as

$$\begin{aligned} \bar{\epsilon}_1 &= \begin{pmatrix} \epsilon_t & 0 & 0 \\ 0 & \epsilon_t & 0 \\ 0 & 0 & \epsilon_z \end{pmatrix}, & \bar{\mu}_1 &= \begin{pmatrix} \mu_t & ig & 0 \\ -ig & \mu_t & 0 \\ 0 & 0 & 1 \end{pmatrix}, \\ \bar{\xi}_1 &= \begin{pmatrix} 0 & 0 & 0 \\ 0 & 0 & 0 \\ 0 & 0 & 0 \end{pmatrix}, \end{aligned} \quad (2)$$

where $\epsilon_z = 1 - \omega_{p1}^2/\omega^2$ is Drude's dispersion [15]. ω_{p1} and ω are the plasma frequency and the angular frequency, respectively. And we assume $\epsilon_t = \mu_t = 1$. Moreover, in the permeability tensor $\bar{\mu}_1$ of Eq. (2), g represents the gyromagnetic parameter. It expresses the degree of time-reversal symmetry breaking. The system obviously destroys the time-reversal symmetry, while holding spatial inversion symmetry.

The constitutive matrices of the chiral metamaterials are expressed as

$$\begin{aligned} \bar{\epsilon}_2 &= \begin{pmatrix} \alpha & 0 & 0 \\ 0 & \alpha & 0 \\ 0 & 0 & \beta \end{pmatrix}, & \bar{\mu}_2 &= \begin{pmatrix} 1 & 0 & 0 \\ 0 & 1 & 0 \\ 0 & 0 & 1 \end{pmatrix}, \\ \bar{\xi}_2 &= \begin{pmatrix} \gamma & 0 & 0 \\ 0 & \gamma & 0 \\ 0 & 0 & 0 \end{pmatrix}, \end{aligned} \quad (3)$$

where $\alpha = 1$, $\beta = 1 - \omega_{p2}^2/\omega^2$ possesses Drude's dispersion. $\omega_{p2} = \sqrt{Ne^2/\epsilon_0 m_{\text{eff}}}$ is also the plasma frequency. N , e , and m_{eff} denote the electron concentration, elementary electron charge, and the effective mass of the electrons, respectively. Moreover, in the chiral tensor $\bar{\xi}_2$ of Eq. (3), γ is the chiral coupling parameter, which corresponds to electromagnetic responses. It should be noted that if chiral metamaterials have the properties of both being hyperbolic (having different signs of the diagonal elements of $\bar{\epsilon}_2$) and chirality (diagonal elements satisfying the relation $\bar{\eta} = -\bar{\xi}$) at the same time, it supports the three-dimensional gapless phase with Weyl points [37].

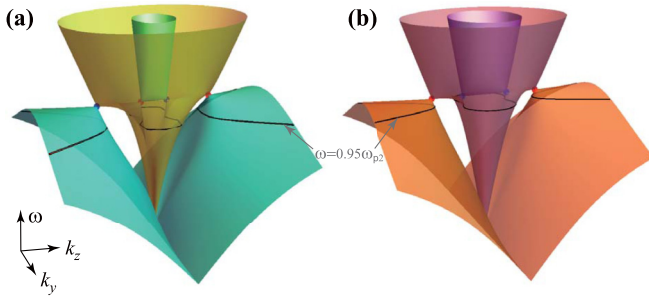


FIG. 1. Band structures diagrams ($k_x = 0$) and the spatial locations of Weyl points for the gyromagnetic and chiral metamaterials, respectively. The red/blue dots indicate Weyl points with positive/negative chirality. The other electromagnetic parameters for (a) are $\epsilon_t = 1$, $\mu_t = 1$, $g = 0.9$, and $\omega_{p1} = 1.09\omega_{p2}$ and for (b) are $\alpha = 1$, $\gamma = 0.4$, and $\omega_{p2} = 1$. The black curves represent equifrequency surfaces with frequency $\omega = 0.95\omega_{p2}$.

For experimental considerations, the gyromagnetic metamaterials in Eq. (2) can be realized by using a periodic multilayered structure of metal layers and ferrite materials based on the effective medium theory [57]. Moreover, by adjusting the thickness of each layer within an appropriate range, the required material parameters can be obtained, such as a larger gyromagnetic effect parameter g . On the other hand, the chiral effects generally can exist in a series of natural materials, and one can synthesize strong chiral media with the development of metamaterials [37]. The chiral metamaterials described by Eq. (3) can be realized by the metallic helical structure [9,15,37]. Particularly, the metallic helical elements are utilized to introduce electric resonance along the z direction, thereby realizing the electric longitudinal mode ($\beta = 1 - \omega_{p2}^2/\omega^2 = 0$). Moreover, the helical elements in the x - y plane need to possess C_4 rotation symmetry to preserve the in-plane isotropic chiral response [26].

We consider the electromagnetic waves with the time-dependent factor $e^{-i\omega t}$. Then, combining $\nabla \times \mathbf{E} = i\omega \mathbf{B}$ and $\nabla \times \mathbf{H} = -i\omega \mathbf{D}$, we introduce the singular antisymmetric tensor matrix:

$$\bar{\kappa} = \begin{pmatrix} 0 & -k_z & k_y \\ k_z & 0 & -k_x \\ -k_y & k_x & 0 \end{pmatrix}. \quad (4)$$

Maxwell's equations with the constitutive relations [Eq. (1)] can be further transformed into the following form (only the part related to the electric field \mathbf{E} is shown here):

$$[(\bar{\kappa} + i\bar{\xi})\bar{\mu}^{-1}(\bar{\kappa} - i\bar{\eta}) + \bar{\epsilon}]\mathbf{E} = 0. \quad (5)$$

The electric field $E = (E_x, E_y, E_z)^T$ can describe the wave propagation in the medium. When the determinant of the square matrix on the left side of Eq. (5) is zero, nontrivial solutions of \mathbf{E} exist, and the characteristic equation is obtained. Then, it yields the band dispersion relation of the metamaterial. In the present paper, we set ω as normalized to the effective plasma frequency ω_{p2} . Moreover, ω_{p1} and ω_{p2} satisfy the relation $\omega_{p1} = 1.09\omega_{p2}$. All the wave vectors $\mathbf{k} = [k_x, k_y, k_z]$ are normalized to wave number k_p ($k_p = \omega/c$).

Figure 1(a) shows the band structures ($k_x = 0$) for the gyromagnetic metamaterial with $\epsilon_t = 1$, $\mu_t = 1$, $g = 0.9$, and

$\omega_{p1} = 1.09\omega_{p2}$. There are four Weyl points with a single topological charge, which are located symmetrically on the k_z axis in the gyromagnetic system, as indicated by red/blue dots in Fig. 1(a). The locations of the two pairs of Weyl points are $(k_x, k_y, k_z) = (0, 0, \pm 0.34)$ and $(0, 0, \pm 1.5)$ with $\omega = \omega_{p1} = 1.09\omega_{p2}$, respectively. The red and blue dots represent the positive chirality ($C = +1$) and the negative chirality ($C = -1$) Weyl points, respectively. In particular, the Weyl point here is produced by the linear crossing of one transverse mode and one longitudinal plasmon mode. The dispersion relations of the transverse modes [21] can be expressed as $k_{z1} = \pm\omega\sqrt{\epsilon_t(g + \mu_t)}$ and $k_{z2} = \pm\omega\sqrt{\epsilon_t(-g + \mu_t)}$. The dispersion of the longitudinal electric mode is determined by $\epsilon_z = 1 - \omega_{p1}^2/\omega^2 = 0$. Notably, since the nonlocal effect of the gyromagnetic metamaterial is not considered, the dispersion of the longitudinal mode is flat, as shown in Fig. 1(a). Hence, the Weyl points of the metamaterial are exactly at the critical transition between the type-I and type-II Weyl points.

As mentioned above, we propose a nonmagnetic ($\bar{\mu}_2 = \bar{I}$) anisotropic homogeneous chiral material. In order to display equifrequency surfaces similar to that of gyromagnetic metamaterials near the Weyl point in chiral systems, we set the electromagnetic parameters of chiral metamaterials as $\alpha = 1$, $\gamma = 0.4$, and $\omega_{p2} = 1$. As shown in Fig. 1(b), the chiral system supports a total of two pairs of Weyl points. All of them carry single monopole charges located symmetrically on the k_z axis. At the Weyl degeneracy frequency $\omega = \omega_{p2}$, there exists one pair of Weyl points in momentum space located at $(0, 0, \pm 1.4)$. They carry positive topological charges, highlighted by the red dots in Fig. 1(b). Another pair of Weyl points close to the origin of the momentum space is located at $(0, 0, \pm 0.6)$, as indicated by the blue dots. Note here that the two Weyl points can be regarded as merged into a double Weyl point with a total topological charge of $C = -2$. In addition, similar to the case of gyromagnetic metamaterials, the Weyl degeneracy points in the chiral system are also critical-type Weyl points. The expression of one of the two bands forming the Weyl point is $\beta = 1 - \omega_{p2}^2/\omega^2 = 0$. Hence, the longitudinal plasmon mode has a flat dispersion relation. From the eigenfield [Eq. (5)] of the chiral metamaterials, we obtain the dispersion relations of the transverse modes as $k_{z3} = \pm\omega(\gamma + \sqrt{\alpha})$, $k_{z4} = \pm\omega(-\gamma + \sqrt{\alpha})$.

In the following analysis, we focus on frequency $\omega = 0.95\omega_{p2}$ for the equifrequency surfaces of the gyromagnetic (GM , $g > 0$) and chiral (CM , $\gamma > 0$) metamaterials. In this situation, the bulk states of two Weyl materials have similar equifrequency contours, which are shown as black curves in Figs. 1(a) and 1(b).

Figure 2(a) illustrates the equifrequency surfaces for the gyromagnetic metamaterials (the cyan curves) and vacuum (the gray dotted line). They possess rotational symmetry about the k_z axis and reflection symmetry about the k_x - k_y plane [57]. The equifrequency surfaces are composed of an elliptical surface and two hyperboloids extending toward infinity. Notably, one pair of Weyl points symmetrically distributed near the origin of momentum space carries the opposite chirality topological charges. Therefore, the total topological charge in the middle closed contour is zero. There will be one Fermi arc on the surface of the Weyl semimetal owing to the bulk-edge correspondence [40,58]. It connects two projections of

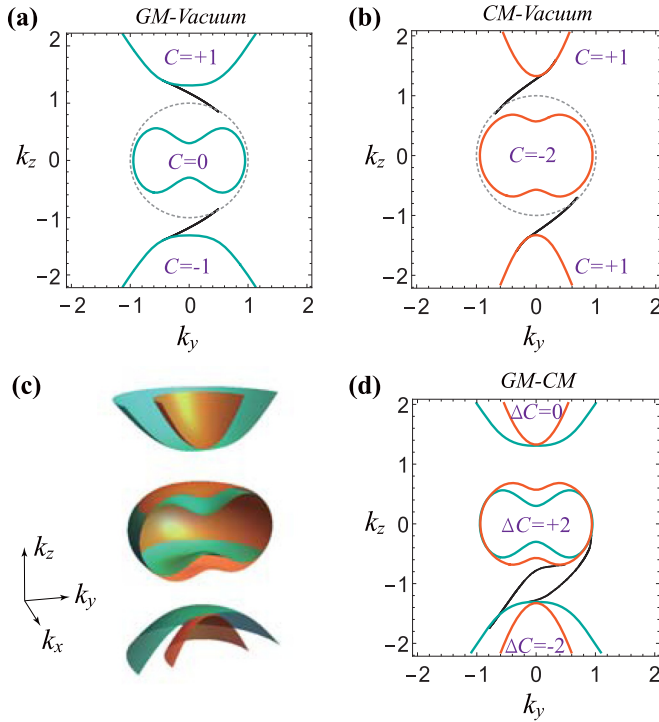


FIG. 2. Equifrequency surfaces of the gyromagnetic and chiral metamaterials. (a), (b) Bulk states and nontrivial Fermi arc surface states (the black curves) between the gyromagnetic (the cyan curves) or chiral (the orange curves) metamaterials ($x < 0$) and vacuum state ($x > 0$) (the gray dotted line), respectively. (c) The three-dimensional equifrequency surfaces ($k_x < 0$ half space) of the gyromagnetic (cyan) and chiral (orange) metamaterials. (d) Bulk states and Fermi arc surface states between the gyromagnetic ($x > 0$) and chiral ($x < 0$) metamaterials.

equifrequency surfaces with different topological charges. The black curve represents the Fermi arc bridging the Weyl points in Fig. 2(a). Due to the presence of spatial inversion symmetry, the Fermi arcs located at $k_z > 0$ and $k_z < 0$ regions are symmetrically distributed.

As exhibited in Fig. 2(b), the equifrequency surface of the chiral metamaterials has a similar equifrequency contour shape to those in the gyromagnetic metamaterials. The orange curves represent the bulk states of the chiral metamaterial. There exist two gaps between a central elliptical and a two sheeted hyperboloid-type surface. Since the Chern number difference between each gap is one, only one Fermi arc (the black curve) will be generated. However, the configurations of the Fermi arcs of the gyromagnetic and chiral metamaterials are extremely different owing to the distinct symmetry-protection mechanisms. As shown in Fig. 2(b), the existence of the time-reversal symmetry of the system ensures that the Fermi arc is symmetrically distributed with regard to the origin of the coordinate.

What novel phenomena will be brought about by considering the interface composed of the above two photonic Weyl metamaterials? We guess that the configurations of Fermi arc surface states on the interface between the gyromagnetic metamaterials and the chiral metamaterials are quite different from Figs. 2(a) and 2(b). To better verify this

conjecture and understand the reason for the difference, we exhibit the equifrequency surfaces and Fermi arcs between different media and conduct a comparative analysis. The three-dimensional bulk states and the nontrivial gap where the topological surface states reside are shown in Fig. 2(c). The cyan and orange surfaces represent the equifrequency surface of the gyromagnetic ($x > 0$) and chiral metamaterials ($x < 0$), respectively. Nontrivial Fermi arc surface states (the black curves) are given in Fig. 2(d). They serve as a signature of the topological nature of the system [59]. Interestingly, there is no Fermi arc surface state passing through the gap in the $+k_z$ region. It means that the $+k_z$ region prohibits any surface modes. In contrast, two Fermi arc surface states exist across the gap in the $-k_z$ part. The reason for this singular behavior is that this system contains two Weyl metamaterials, which requires consideration of the difference in the Chern numbers of the two media on both sides of the boundary [Fig. 2(d)]. As identified in Figs. 2(a) and 2(b), the two hyperbolic parts located in the $+k_z$ space have the same Chern number of $C = +1$. The Chern number difference between the two Weyl media is $\Delta C = C_{GM} - C_{CM} = 0$, as illustrated in Fig. 2(d). Therefore, no Fermi arc is allowed in the $+k_z$ gap. Nevertheless, the two hyperbolic branches in the $-k_z$ space possess unequal Chern numbers; their difference is $\Delta C = C_{GM} - C_{CM} = -2$. According to the bulk-edge correspondence, there are two Fermi arcs in the $-k_z$ gap, and the Fermi arc surface states will be tangent to the corresponding bulk states.

III. DISORDER-IMMUNE FERMION ARC AND MULTIPLEXING PHOTONIC ROUTING

As mentioned before, for the system involving two photonic Weyl semimetals, two exotic nonclosed Fermi arcs are allowed to exist [Fig. 2(d)]. These Fermi arcs are protected by the topological charge associated with the Weyl points. This reveals the characteristic features of topological Weyl semimetals [44,60]. To demonstrate the topological nontriviality of the Fermi arcs, COMSOL MULTIPHYSICS is used to study the excitation and propagation of surface waves. As shown in Fig. 3(a), we set the x direction as the normal of the interface between the gyromagnetic ($x > 0$) and chiral metamaterials ($x < 0$). The angular frequency ω is a constant (ω is normalized to ω_{p2}) because we study Fermi arcs on the equal frequency surfaces. In this case, the material system contains only the variables k_y and k_z in the wave vector space. Then, the two-dimensional frequency-domain simulations are performed in the x - y plane for Fermi arcs with different propagation constants k_z in the gap [Fig. 2(d)]. We set scattering boundary conditions in the x and y directions. Moreover, the electromagnetic waves ($k_z = -1.1$) can be excited by the electric dipole sources located at the boundary of gyromagnetic and chiral metamaterials, which are marked by the black stars, as depicted in Fig. 3. Since both Fermi arcs have the group velocities of $+y$ components, the corresponding surface waves can propagate in the $+y$ direction. This means that the two Fermi arc surface states have the same propagation directions.

The disorder-immune transmission characteristics of the Fermi arc surface states are demonstrated by different shapes and different numbers of defects on the interface. As exhibited

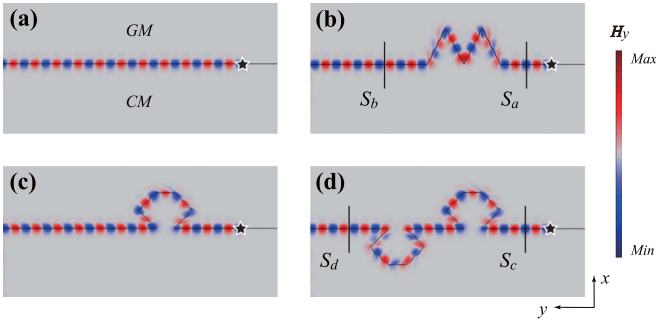


FIG. 3. The disorder-immune wave propagations on the interfaces between the gyromagnetic ($x > 0$) and chiral ($x < 0$) metamaterials. Simulated wave propagations along the different types and numbers of defects for $k_z = -1.1$ in Fig. 2(d): (a) the straight case, (b) the M-shaped channel, (c) the Ω -shaped channel, and (d) the double Ω -shaped channel. The black stars are marked for the position of the electric dipole sources to excite electromagnetic waves. The H_y field distributions are obtained by COMSOL numerical simulation and share the same color map. The energy flows of surface waves before and after passing through the defects are indicated by $S_a(S_c)$ and $S_b(S_d)$, respectively.

in Figs. 3(b) and 3(c), whether they encounter one M-shaped defect or one Ω -shaped defect, the surface waves can achieve unidirectional transmission without reflection. Then, we also consider the impact of the number of defects. As shown in Fig. 3(d), two Ω -shaped defects are introduced at the interface, and surface waves can still bypass them for robust transmission. The energy flows of surface waves before and

after passing through the defects are indicated by $S_a(S_c)$ and $S_b(S_d)$, respectively, as shown in Figs. 3(b) and 3(d). Numerical calculations show that the energy of surface waves is conserved after experiencing different shapes and numbers of defects ($S_b/S_a = S_d/S_c = 1$). Thus, it is demonstrated that the Fermi arc surface states are immune to defects. This unique disorder-immune transmission feature can give birth to enormous potential applications, especially in multichannel information unidirectional transportation.

The existence of multiple copropagating topological channels may bring many fascinating possible future applications. Here, based on the demonstrated propagation of the multiple surface states signals, we will show how the one-way surface states signals can be combined or split at the H junction. As plotted in Fig. 4(a), the H-shaped interface we designed consists of the gyromagnetic and chiral metamaterials and the vacuum. Two electric dipole sources (S_1 and S_2) excite electromagnetic waves, indicated by the black stars at two different locations on the right-hand side, as shown in Fig. 4(b). At the interface between the gyromagnetic/chiral metamaterials and vacuum, it is noted that only one Fermi arc surface state is allowed in both $+k_z$ and $-k_z$ regions in Figs. 2(a) and 2(b). Nevertheless, at the interface between the gyromagnetic and chiral metamaterials, only the $-k_z$ space is allowed to have two copropagating photonic Fermi arcs [Fig. 2(d)]. Consequently, we choose the negative propagation constant to analyze surface waves, i.e., $k_z = -1.1$. As illustrated in Fig. 4(b), two surface waves are emitted from the top and bottom ports on the right-hand side, and are merged into a common channel at the interface of the middle part. Then, they are divided into two opposite propagating paths on

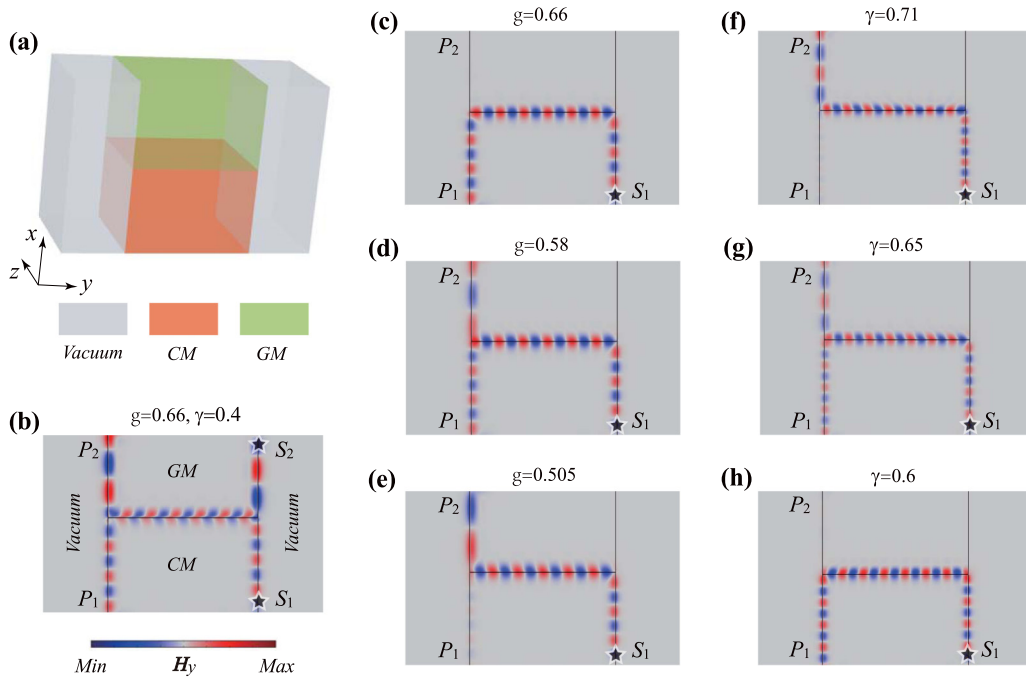


FIG. 4. Fermi arc surface states combiner and splitter. (a) Three-dimensional schematics of surface waves across the H junction. (b) Copropagating channels for surface waves multiplexing and division. The black stars on the right-hand side represent two excitation sources (S_1 and S_2) at two different locations, which excite electromagnetic waves with $k_z = -1.1$. (c)–(e) The wave transportation under different gyromagnetic parameters when chiral parameter $\gamma = 0.4$. (f)–(h) The chiral parameter γ varies, but the gyromagnetic parameter $g = 0.9$ remains unchanged.

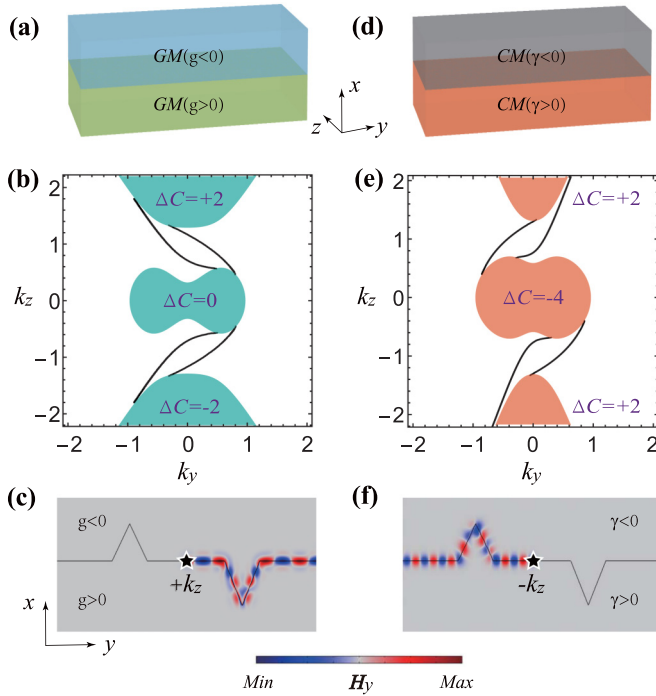


FIG. 5. Bulk states, Fermi arcs, and nonreciprocal propagation of the surface waves. (a), (d) Three-dimensional schematics of two topological Weyl metamaterials. (b), (e) Bulk states (the cyan and orange parts, respectively) and Fermi arc surface states (the black curves) between the gyromagnetic ($g < 0$ and $g > 0$) and chiral metamaterials ($\gamma < 0$ and $\gamma > 0$). (c), (f) Simulated surface waves transportation under the x - y view of (a) and (d), respectively. The signs of propagation constant k_z are given in the diagram.

the left-hand side and output by two output ports respectively (P_1 and P_2).

Next, we only excite the surface wave at one input port (S_1 is retained). As shown by Figs. 4(c)–4(e), when the chiral parameter γ is fixed ($\gamma = 0.4$), the wave transport is studied under different gyromagnetic parameters g . From the numerical simulation results, it can be clearly seen that at the output ports, the wave can only flow to the P_1 port in Fig. 4(c), or there is energy outflow at P_1 and P_2 [Fig. 4(d)], or nearly all flow to the P_2 port [shown as Fig. 4(e)]. A similar phenomenon also occurs in Figs. 4(f)–4(h) where g is fixed ($g = 0.9$) but γ varies. This unique property may find applications in signal combiner and splitter, controllable routing, optical switches, optical isolation devices, and so on.

IV. MULTICHANNEL FERMION ARC AND NONRECIPROCAL PROPAGATION OF SURFACE WAVES

Here, we study the presence of two exotic Fermi arcs in the nontrivial common gap between two topological Weyl metamaterials. As illustrated in Figs. 5(a) and 5(d), three-dimensional schematics of the gyromagnetic ($g < 0$ and $g > 0$) and chiral metamaterials are given ($\gamma < 0$ and $\gamma > 0$), respectively. The two systems achieve a higher gap Chern number. As shown in Figs. 5(b) and 5(e), there are two Fermi arcs across in the $+k_z$ gap and $-k_z$ gap, which

satisfies the bulk-edge correspondence. In particular, because the two Weyl systems have spatial inversion and time-reversal symmetry invariant, respectively, the configurations of the corresponding Fermi arcs are quite different. In order to verify that the surface modes are allowed to exist in both $+k_z$ space and $-k_z$ space, we separately excite surface waves with propagation constants of opposite signs. Numerical simulations show that these surface waves propagate robustly in one direction, without scattering or reflection at the corners, as shown in Figs. 5(c) and 5(f).

The Fermi arc surface states have interesting applications, especially in unidirectional waveguides and nonreciprocal transmission functional devices. It is possible to construct a T-shaped interface configuration by reasonably arranging the gyromagnetic, the chiral, and the reversed chiral metamaterials (r -CM, meaning that the sign of γ is reversed, i.e., $\gamma < 0$). As illustrated by Figs. 6(a) and 6(d), we show the three-dimensional schematic diagrams of a T-shaped interface composed of three topological Weyl media. The colored arrows indicate the direction of propagation of the surface waves. The metamaterial types are labeled by the colored squares at the bottom.

As shown in Figs. 6(b) and 6(c), in order to verify the nonreciprocity properties of surface waves, the excitation sources are placed at different positions for simulation. We adopt the propagation constant k_z of different signs. Note that points A, B, and C are the excitation sources located at a certain position on the interface of different materials. As exhibited in Fig. 6(b), when the source is placed at point B and the surface waves with $-k_z$ are excited, the surface waves propagate upward and then turn left to output. Notably, when the source is placed at point A and excites the surface waves with $+k_z$, the waves cannot propagate relatively along the original path to B, but go straight to the right and flow out from point C, as shown in Fig. 6(c). To further illustrate the multichannel configuration between the three topological Weyl semimetals, we change the positions of the gyromagnetic and the chiral metamaterials, as indicated in Figs. 6(e) and 6(f). This nonreciprocal propagation characteristic has been well verified and may be used as controllable robust information transportation in the future.

V. EXISTENCE OF WEYL EXCEPTIONAL CONTOURS AND PHASE DIAGRAMS IN WEYL METAMATERIALS WHILE CONSIDERING LOSSES

As with most previous studies of Weyl materials in photonic and acoustic systems [15,24], we ignored losses in the preceding discussion. However, the nature of these classical wave systems is dissipative losses. Generally, in the presence of non-Hermitian perturbations (losses), a conventional Weyl point will transform into a closed contour of an exceptional point with the same topological charge, which is called the Weyl exceptional contour [16,61–64]. In addition, the size of the formed Weyl exceptional contours depends on the magnitude of the non-Hermitian perturbation, and the size of Weyl exceptional contours is monotonically related to the losses in the system [16].

In order to quantitatively analyze the effect of losses on the topological properties of Weyl materials, we consider

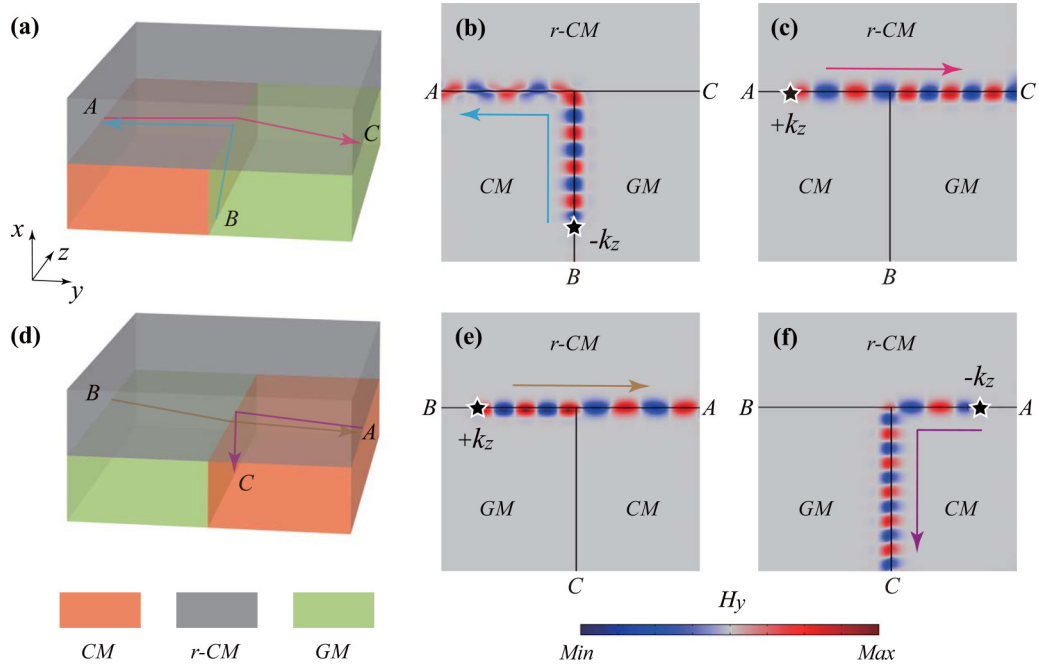


FIG. 6. Nonreciprocal topological Fermi arc surface states on the T-junction waveguide. (a), (d) Three-dimensional schematic diagrams of the T-shaped interface configuration composed of three topological Weyl media. The metamaterial types are marked with colored squares at the bottom. (b), (c) Simulated surface waves transportation on the x - y plane of (a). (e), (f) Similar results to (b) and (c), but corresponding to the T-junction structure of (d). The panels show the signs of the propagation constant k_z . The colored arrows represent the surface waves propagating directions.

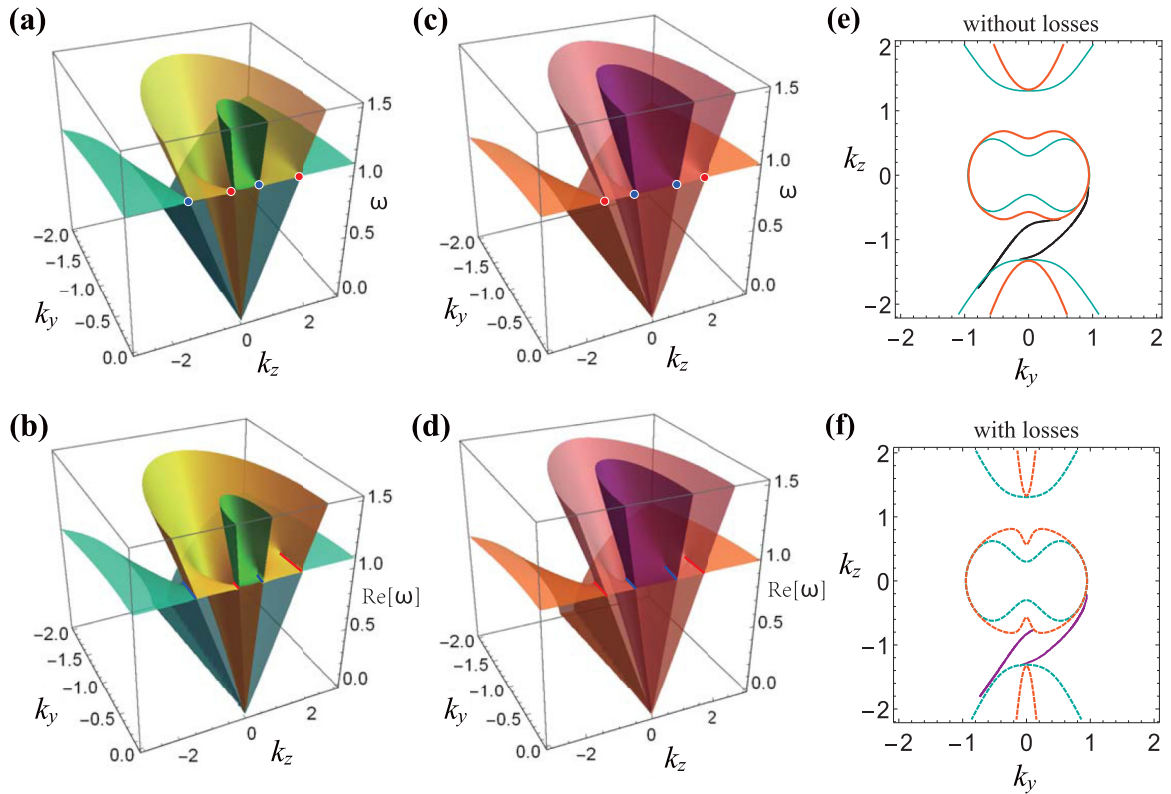


FIG. 7. (a), (c) Band structures ($k_x = 0$) for the gyromagnetic and chiral metamaterials without considering losses, respectively. The electromagnetic parameters for (a) are $\epsilon_r = 1$, $\mu_r = 1$, $g = 0.9$, and $\omega_{p1} = 1.09\omega_{p2}$ and for (c) are $\alpha = 1$, $\gamma = 0.4$, and $\omega_{p2} = 1$. (b), (d) Band structures ($k_x = 0$) for the gyromagnetic and chiral metamaterials with considering losses, respectively. The parameters in (b) and (d) are the same as those in (a) and (c), respectively, but the losses terms are added, i.e., (b) $\tau = 0.3$ and (d) $\eta = 0.3$. (e), (f) Fermi arc surface states (the black and purple solid lines) on the interface between the gyromagnetic ($x > 0$) and chiral ($x < 0$) metamaterials without and with losses scenarios, respectively.

the Drude models with losses: $\epsilon_z = 1 - \omega_{p1}^2/[\omega(\omega + i\tau)]$ and $\beta = 1 - \omega_{p2}^2/[\omega(\omega + i\eta)]$ in gyromagnetic and chiral metamaterials, respectively [65]. Here, τ and η are damping terms representing losses. Moreover, τ and η are normalized to ω_{p2} . Without losing generality, we set $\tau = 0.3$ and $\eta = 0.3$ [62,66].

As illustrated in Figs. 7(a)–7(d), we give the bulk structures ($k_x = 0$) without and with losses in the half space $k_y < 0$, respectively. Specifically, Figs. 7(a) and 7(c) are the cases without considering the losses, and the electromagnetic parameters used are the same as those in Figs. 2(a) and 2(b), respectively. There are four Weyl points symmetrically located on the k_z axis in gyromagnetic and chiral metamaterials. The red and blue dots indicate the positive and negative chirality Weyl points, respectively.

On the other hand, while taking the losses into account ($\tau = 0.3$ and $\eta = 0.3$), the Weyl point transforms into the Weyl exceptional contour carrying the same topological charge in gyromagnetic and chiral metamaterials, respectively, as shown in Figs. 7(b) and 7(d). These Weyl exceptional contours are also symmetrically distributed along the k_z axis. The red/blue curves represent the Weyl exceptional contours with the positive/negative chirality.

Moreover, it should be noted that both Weyl points and Weyl exceptional contours result from the band degeneracy in three-dimensional space. Similar to the case of Weyl points, Weyl exceptional contours not only have topological charges but also preserve Fermi arc surface states. As indicated in Figs. 7(e) and 7(f), we give the Fermi arc surface states (the black and purple solid lines) between the gyromagnetic ($x > 0$) and chiral ($x < 0$) metamaterials without and with losses scenarios, respectively. Notably, under the non-Hermitian perturbation in the gyromagnetic and chiral metamaterials, there are still two copropagating Fermi arc surface states in the system [Fig. 7(f)]. Although considering the losses in Weyl metamaterials will change the band structure, we clarify that the copropagating Fermi arc surface state still exists in Fig. 7.

Generally, in the presence of non-Hermitian perturbation, the losses will affect the size and spatial position of the Weyl exceptional contour. Particularly, with increasing the losses of the system, if any point on one Weyl exceptional contour is in contact with a point on another Weyl exceptional contour with opposite topological charge, the two Weyl exceptional contours will dissipate their charge and the system will undergo a topological transition to a trivial phase [64]. Therefore, to quantitatively study the robustness of the Weyl semimetal phase to the effect of losses, we further explore and discuss the phase diagram in the gyromagnetic and chiral metamaterials while considering the losses, as shown in Fig. 8.

The cyan/orange and gray shaded areas indicate the presence and absence of Weyl exceptional contours of the gyromagnetic/chiral metamaterials with losses respectively, as illustrated in Figs. 8(a) and 8(c). The Weyl semimetal phase possesses the Weyl exceptional contours and the Fermi arc surface states. In contrast, the trivial phase does not have these exotic states and has zero total topological charges. The black lines represent the critical values at which two Weyl exceptional contours with opposite topological charges in-

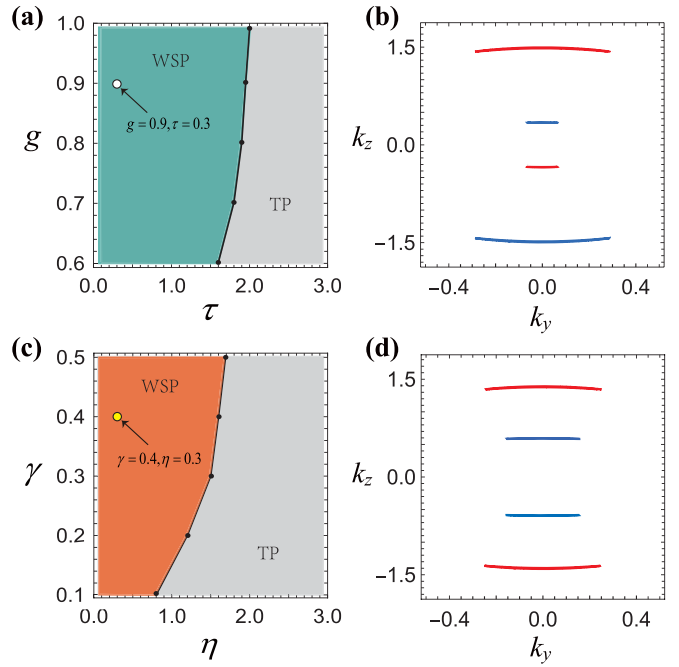


FIG. 8. (a), (c) Phase diagrams for the gyromagnetic and chiral metamaterials with considering losses. The Weyl semimetal phase and trivial phase are represented by WSP and TP, respectively. (b), (d) Weyl exceptional contours of gyromagnetic ($g = 0.9$, $\tau = 0.3$) and chiral metamaterials ($\gamma = 0.4$, $\eta = 0.3$) in the k_y - k_z plane, respectively. The red and blue curves indicate the Weyl exceptional contours carrying positive and negative chirality, respectively.

intersect for annihilation. As shown in Figs. 8(b) and 8(d), we give the Weyl exceptional contours of the gyromagnetic metamaterial ($g = 0.9$, $\tau = 0.3$) and the chiral metamaterial ($\gamma = 0.4$, $\eta = 0.3$) in the k_y - k_z plane, respectively. The four Weyl exceptional contours caused by losses are symmetrically distributed on the k_z axis. The red and blue curves indicate the Weyl exceptional contours with positive and negative chirality, respectively. Moreover, for the gyromagnetic and chiral metamaterials, the topology of the system is changed (the Weyl semimetal phase transitions to the trivial phase) when losses are the same order of magnitude as the plasma frequency ω_{p2} , as shown by the black lines in Figs. 8(a) and 8(c). However, such a level of losses is unrealistic for the Drude medium models [16]. Thus, when analyzing the copropagating Fermi arc surface states, the influence of losses in the gyromagnetic/chiral metamaterials can be ignored [Eqs. (2) and (3)].

VI. CONCLUSIONS

In conclusion, we demonstrated that the photonic system containing two Weyl metamaterials with different symmetry-protection mechanisms can support the copropagating Fermi arc surface states. The dispersion relations of the two bands forming the photonic Weyl degeneracies are presented. For the system possessing multiple surface states, it is necessary to select the gyromagnetic and chiral metamaterials with similar equifrequency surfaces. According to the bulk-edge correspondence, two nontrivial Fermi arc surface states holding

identical propagation directions can surprisingly occur at the interface between two different photonic Weyl metamaterials. However, due to the distinct symmetry-protection mechanism, the configurations of the Fermi arcs of the gyromagnetic and chiral metamaterials are extremely different. In addition, we proved theoretically that the Fermi arcs are protected by the underlying topology. The surface waves are not affected by the number and shape of defects and can be one-way robustly transmitted. By using different interfaces, we realized the control of the nonreciprocal transmission of surface waves and the controllable routing of energy flow. In particular, the splitting and merging phenomena of the surface states in the H-junction cross waveguides are realized. Multichannel topological transport of the disorder-immune Fermi arcs is demonstrated and verified by simulations in a T-junction

interface configuration. Interestingly, we show the existence of Weyl exceptional contours in gyromagnetic and chiral metamaterials with losses and analyze the phase diagrams for the system transition from a Weyl semimetal phase to a trivial phase. Our paper is helpful to clarify the copropagating photonic Fermi arc surface states and their transport properties at the interface between two different Weyl materials.

ACKNOWLEDGMENT

This work was financially supported by the National Natural Science Foundation of China under Grant No. 62075048 and the Natural Science Foundation of Shandong Province under Grant No. ZR2020MF129.

-
- [1] P. Hosur and X.-L. Qi, Recent developments in transport phenomena in Weyl semimetals, *C. R. Phys.* **14**, 857 (2013).
- [2] J. Hu, S. Xu, N. Ni, and Z. Mao, Transport of topological semimetals, *Annu. Rev. Mater. Res.* **49**, 207 (2019).
- [3] Z. Yu, Y. Yao, and S. A. Yang, Predicted Unusual Magnetoresponse in Type-II Weyl Semimetals, *Phys. Rev. Lett.* **117**, 077202 (2016).
- [4] B. A. Bernevig, It's been a Weyl coming, *Nat. Phys.* **11**, 698 (2015).
- [5] A. Westström and T. Ojanen, Designer Curved-Space Geometry for Relativistic Fermions in Weyl Metamaterials, *Phys. Rev. X* **7**, 041026 (2017).
- [6] B. Q. Lv, H. M. Weng, B. B. Fu, X. P. Wang, H. Miao, J. Ma, P. Richard, X. C. Huang, L. X. Zhao, G. F. Chen, Z. Fang, X. Dai, T. Qian, and H. Ding, Experimental Discovery of Weyl Semimetal TaAs, *Phys. Rev. X* **5**, 031013 (2015).
- [7] L. Lu, L. Fu, J. D. Joannopoulos, and M. Soljačić, Weyl points and line nodes in gyroid photonic crystals, *Nat. Photon.* **7**, 294 (2013).
- [8] L. Lu, Z. Wang, D. Ye, L. Ran, L. Fu, J. D. Joannopoulos, and M. Soljačić, Experimental observation of Weyl points, *Science* **349**, 622 (2015).
- [9] Y. Yang, Z. Gao, X. Feng, Y. Huang, P. Zhou, S. A. Yang, Y. Chong, and B. Zhang, Ideal Unconventional Weyl Point in a Chiral Photonic Metamaterial, *Phys. Rev. Lett.* **125**, 143001 (2020).
- [10] X. Huang, W. Deng, F. Li, J. Lu, and Z. Liu, Ideal Type-II Weyl Phase and Topological Transition in Phononic Crystals, *Phys. Rev. Lett.* **124**, 206802 (2020).
- [11] X. Fan, C. Qiu, Y. Shen, H. He, M. Xiao, M. Ke, and Z. Liu, Probing Weyl Physics with One-Dimensional Sonic Crystals, *Phys. Rev. Lett.* **122**, 136802 (2019).
- [12] F. Li, X. Huang, J. Lu, J. Ma, and Z. Liu, Weyl points and Fermi arcs in a chiral phononic crystal, *Nat. Phys.* **14**, 30 (2018).
- [13] A. A. Burkov, Topological semimetals, *Nat. Mater.* **15**, 1145 (2016).
- [14] B. Yan and C. Felser, Topological materials: Weyl semimetals, *Annu. Rev. Condens. Matter Phys.* **8**, 337 (2017).
- [15] M. Xiao, Q. Lin, and S. Fan, Hyperbolic Weyl Point in Reciprocal Chiral Metamaterials, *Phys. Rev. Lett.* **117**, 057401 (2016).
- [16] K. Shastri and F. Monticone, Dissipation-induced topological transitions in continuous Weyl materials, *Phys. Rev. Research* **2**, 033065 (2020).
- [17] Q. Wang, Y. Ge, H. Sun, H. Xue, D. Jia, Y. Guan, S. Yuan, B. Zhang, and Y. D. Chong, Vortex states in an acoustic Weyl crystal with a topological lattice defect, *Nat. Commun.* **12**, 3654 (2021).
- [18] M. Chang, M. Xiao, W. Chen, and C. T. Chan, Multiple Weyl points and the sign change of their topological charges in woodpile photonic crystals, *Phys. Rev. B* **95**, 125136 (2017).
- [19] X. Wan, A. M. Turner, A. Vishwanath, and S. Y. Savrasov, Topological semimetal and Fermi-arc surface states in the electronic structure of pyrochlore iridates, *Phys. Rev. B* **83**, 205101 (2011).
- [20] Ş. K. Özdemir, Fermi arcs connect topological degeneracies, *Science* **359**, 995 (2018).
- [21] M. Li, J. Song, and Y. Jiang, Photonic topological Weyl degeneracies and ideal type-I Weyl points in the gyromagnetic metamaterials, *Phys. Rev. B* **103**, 045307 (2021).
- [22] D. Wang, B. Yang, W. Gao, H. Jia, Q. Yang, X. Chen, M. Wei, C. Liu, M. Navarro-Cía, J. Han, W. Zhang, and S. Zhang, Photonic Weyl points due to broken time-reversal symmetry in magnetized semiconductor, *Nat. Phys.* **15**, 1150 (2019).
- [23] H. B. Nielsen and M. Ninomiya, Absence of neutrinos on a lattice: (I). Proof by homotopy *Nucl. Phys. B* **185**, 20 (1981).
- [24] W. Gao, B. Yang, M. Lawrence, F. Fang, B. Béni, and S. Zhang, Photonic Weyl degeneracies in magnetized plasma, *Nat. Commun.* **7**, 12435 (2016).
- [25] J. Noh, S. Huang, D. Leykam, Y. D. Chong, K. P. Chen, and M. C. Rechtsman, Experimental observation of optical Weyl points and Fermi arc-like surface states, *Nat. Phys.* **13**, 611 (2017).
- [26] J. Guo, B. Yang, S. Ma, H. Chan, G. Situ, and S. Zhang, Copropagating photonic Fermi arc channels for multiplexing and dynamically routing topological surface waves, *Laser Photon. Rev.* **15**, 2000360 (2021).
- [27] W. Chen, M. Xiao, and C. T. Chan, Photonic crystals possessing multiple Weyl points and the experimental observation of robust surface states, *Nat. Commun.* **7**, 13038 (2016).
- [28] N. P. Armitage, E. J. Mele, and A. Vishwanath, Weyl and Dirac semimetals in three-dimensional solids, *Rev. Mod. Phys.* **90**, 015001 (2018).
- [29] A. A. Burkov, Weyl metals, *Annu. Rev. Condens. Matter Phys.* **9**, 359 (2018).
- [30] F. Zangeneh-Nejad and R. Fleury, Zero-Index Weyl Metamaterials, *Phys. Rev. Lett.* **125**, 054301 (2020).

- [31] E. Goi, Z. J. Yue, B. P. Cumming, and M. Gu, Observation of type I photonic Weyl points in optical frequencies, *Laser Photon. Rev.* **12**, 1700271 (2018).
- [32] A. A. Soluyanov, D. Gresch, Z. Wang, Q. Wu, M. Troyer, X. Dai, and B. A. Bernevig, Type-II Weyl semimetals, *Nature (London)* **527**, 495 (2015).
- [33] J. Jiang, Z. K. Liu, Y. Sun, H. F. Yang, C. R. Rajamathi, Y. P. Qi, L. X. Yang, C. Chen, H. Peng, C.-C. Hwang, S. Z. Sun, S.-K. Mo, I. Vobornik, J. Fujii, S. S. P. Parkin, C. Felser, B. H. Yan, and Y. L. Chen, Signature of type-II Weyl semimetal phase in MoTe₂, *Nat. Commun.* **8**, 13973 (2017).
- [34] M. Li, J. Song, and Y. Jiang, Topological characteristic of Weyl degeneracies in a reciprocal chiral metamaterials system, *New J. Phys.* **23**, 093036 (2021).
- [35] Y. Yang, H. Sun, J. Xia, H. Xue, Z. Gao, Y. Ge, D. Jia, S. Yuan, Y. Chong, and B. Zhang, Topological triply degenerate point with double Fermi arcs, *Nat. Phys.* **15**, 645 (2019).
- [36] Q. Jiang, H. Jiang, H. Liu, Q. Sun, and X. C. Xie, Topological Imbert-Fedorov Shift in Weyl Semimetals, *Phys. Rev. Lett.* **115**, 156602 (2015).
- [37] M. Kim, Z. Jacob, and J. Rho, Recent advances in 2D, 3D and higher-order topological photonics, *Light Sci. Appl.* **9**, 130 (2020).
- [38] M. Li, J. Song, and Y. Jiang, Coexistence of topological type-II Weyl and triply degenerate points in a chiral photonic metamaterial, *Phys. Rev. B* **105**, 085304 (2022).
- [39] N. Morali, R. Batabyal, P. K. Nag, E. Liu, Q. Xu, Y. Sun, B. Yan, C. Felser, N. Avraham, and H. Beidenkopf, Fermi-arc diversity on surface terminations of the magnetic Weyl semimetal Co₃Sn₂S₂, *Science* **365**, 1286 (2019).
- [40] Y. Fu and H. Qin, Topological phases and bulk-edge correspondence of magnetized cold plasmas, *Nat. Commun.* **12**, 3924 (2021).
- [41] R. Batabyal, N. Morali, N. Avraham, Y. Sun, M. Schmidt, C. Felser, A. Stern, B. Yan, and H. Beidenkopf, Visualizing weakly bound surface Fermi arcs and their correspondence to bulk Weyl fermions, *Sci. Adv.* **2**, e1600709 (2016).
- [42] L. Xia, W. Gao, B. Yang, Q. Guo, H. Liu, J. Han, W. Zhang, and S. Zhang, Stretchable photonic “Fermi arcs” in twisted magnetized plasma, *Laser Photon. Rev.* **12**, 1700226 (2018).
- [43] S. Xu, C. Liu, S. K. Kushwaha, R. Sankar, J. W. Krizan, I. Belopolski, M. Neupane, G. Bian, N. Alidoust, T. Chang, Horng-T. Jeng, C. Huang, W. Tsai, H. Lin, P. P. Shibayev, F. Chou, R. J. Cava, and M. Z. Hasan, Observation of Fermi arc surface states in a topological metal, *Science* **347**, 294 (2015).
- [44] S. Xu, I. Belopolski, N. Alidoust, M. Neupane, G. Bian, C. Zhang, R. Sankar, G. Chang, Z. Yuan, C. Lee, S. Huang, H. Zheng, J. Ma, D. S. Sanchez, B. Wang, A. Bansil, F. Chou, P. P. Shibayev, H. Lin, S. Jia, and M. Z. Hasan, Discovery of a Weyl fermion semimetal and topological Fermi arcs, *Science* **349**, 613 (2015).
- [45] A. C. Potter, I. Kimchi, and A. Vishwanath, Quantum oscillations from surface Fermi arcs in Weyl and Dirac semimetals, *Nat. Commun.* **5**, 5161 (2014).
- [46] C. Zhang, S. Xu, I. Belopolski, Z. Yuan, Z. Lin, B. Tong, G. Bian, N. Alidoust, C. Lee, S. Huang, T. Chang, G. Chang, C. Hsu, H. Jeng, M. Neupane, D. S. Sanchez, H. Zheng, J. Wang, H. Lin, C. Zhang, H. Lu, S. Shen, T. Neupert, M. Z. Hasan, and S. Jia, Signatures of the Adler-Bell-Jackiw chiral anomaly in a Weyl fermion semimetal, *Nat. Commun.* **7**, 10735 (2016).
- [47] H. He, C. Qiu, L. Ye, X. Cai, X. Fan, M. Ke, F. Zhang, and Z. Liu, Topological negative refraction of surface acoustic waves in a Weyl phononic crystal, *Nature (London)* **560**, 61 (2018).
- [48] H. Cheng, W. Gao, Y. Bi, W. Liu, Z. Li, Q. Guo, Y. Yang, O. You, J. Feng, H. Sun, J. Tian, S. Chen, and S. Zhang, Vortical Reflection and Spiraling Fermi Arcs with Weyl Metamaterials, *Phys. Rev. Lett.* **125**, 093904 (2020).
- [49] L. Lu, H. Gao, and Z. Wang, Topological one-way fiber of second Chern number, *Nat. Commun.* **9**, 5384 (2018).
- [50] N. Wang, R. Zhang, Q. Guo, S. Wang, G. Wang, and C. T. Chan, Optical pulling using topologically protected one way transport surface-arc waves, *Phys. Rev. B* **105**, 014104 (2022).
- [51] L. Luo, H. Wang, Z. Lin, B. Jiang, Y. Wu, F. Li, and J. Jiang, Observation of a phononic higher-order Weyl semimetal, *Nat. Mater.* **20**, 794 (2021).
- [52] H. X. Wang, Z. K. Lin, B. Jiang, G. Y. Guo, and J. H. Jiang, Higher-Order Weyl Semimetals, *Phys. Rev. Lett.* **125**, 146401 (2020).
- [53] R. Wang, B. Xia, Z. Chen, B. Zheng, Y. Zhao, and H. Xu, Symmetry-Protected Topological Triangular Weyl Complex, *Phys. Rev. Lett.* **124**, 105303 (2020).
- [54] A. J. Viitanen, A. Sihvola, I. V. Lindell, and S. Tretyakov, *Electromagnetic Waves in Chiral and Bi-Isotropic Media* (Artech Print, Artech House, 1994).
- [55] S. S. Oh and O. Hess, Chiral metamaterials: Enhancement and control of optical activity and circular dichroism, *Nano Converg.* **2**, 24 (2015).
- [56] Z. Wang, Y. Chong, J. D. Joannopoulos, and M. Soljačić, Observation of unidirectional backscattering-immune topological electromagnetic states, *Nature (London)* **461**, 772 (2009).
- [57] R. Shiu, H. Chan, H. X. Wang, and G. Y. Guo, Photonic Chern insulators made of gyromagnetic hyperbolic metamaterials, *Phys. Rev. Materials* **4**, 065202 (2020).
- [58] K. Imura and Y. Takane, Spin Berry phase in the Fermi-arc states, *Phys. Rev. B* **84**, 245415 (2011).
- [59] B. Yang, Q. Guo, B. Tremain, L. E. Barr, W. Gao, H. Liu, B. Béri, Y. Xiang, D. Fan, A. P. Hibbins, and S. Zhang, Direct observation of topological surface-state arcs in photonic metamaterials, *Nat. Commun.* **8**, 97 (2017).
- [60] S. Jia, S. Xu, and M. Z. Hasan, Weyl semimetals, Fermi arcs and chiral anomalies, *Nat. Mater.* **15**, 1140 (2016).
- [61] Y. Xu, S. Wang, and L. Duan, Weyl Exceptional Rings in a Three-Dimensional Dissipative Cold Atomic Gas, *Phys. Rev. Lett.* **118**, 045701 (2017).
- [62] A. Cerjan, S. Huang, M. Wang, K. P. Chen, Y. Chong, and M. C. Rechtsman, Experimental realization of a Weyl exceptional ring, *Nat. Photon.* **13**, 623 (2019).
- [63] Q. Yan, Q. Chen, L. Zhang, R. Xi, H. Chen, and Y. Yang, Unconventional Weyl exceptional contours in non-Hermitian photonic continua, *Photon. Res.* **9**, 2435 (2021).
- [64] A. Cerjan, M. Xiao, L. Yuan, and S. Fan, Effects of non-Hermitian perturbations on Weyl Hamiltonians with arbitrary topological charges, *Phys. Rev. B* **97**, 075128 (2018).
- [65] J. Pendry, A. Holden, W. Stewart, and I. Youngs, Extremely Low Frequency Plasmons in Metallic Mesostructures, *Phys. Rev. Lett.* **76**, 4773 (1996).
- [66] W. Wang, W. Gao, L. Cao, Y. Xiang, and S. Zhang, Photonic topological fermi nodal disk in non-Hermitian magnetic plasma, *Light Sci. Appl.* **9**, 40 (2020).